

Nature of Nitrogen Incorporation in BiVO₄ Photoanodes through Chemical and Physical Methods

Rowshanak Irani, Ibbi Y. Ahmet, Ji-Wook Jang, Sean P. Berglund, Paul Plate, Christian Höhn, Roman Böttger, Sebastian W. Schmitt, Catherine Dubourdieu, Sheikha Lardhi, Luigi Cavallo, Moussab Harb, Peter Bogdanoff, Roel van de Krol, and Fatwa F. Abdi*


In recent years, BiVO₄ has been optimized as a photoanode material to produce photocurrent densities close to its theoretical maximum under AM1.5 solar illumination. Its performance is, therefore, limited by its 2.4 eV bandgap. Herein, nitrogen is incorporated into BiVO₄ to shift the valence band position to higher energies and thereby decreases the bandgap. Two different approaches are investigated: modification of the precursors for the spray pyrolysis recipe and post-deposition nitrogen ion implantation. Both methods result in a slight red shift of the BiVO₄ bandgap and optical absorption onset. Although previous reports on N-modified BiVO₄ assumed individual nitrogen atoms to substitute for oxygen, X-ray photoelectron spectroscopy on the samples reveals the presence of molecular nitrogen (i.e., N₂). Density functional theory calculations confirm the thermodynamic stability of the incorporation and reveal that N₂ coordinates to two vanadium atoms in a bridging configuration. Unfortunately, nitrogen incorporation also results in the formation of a localized state of ≈0.1 eV below the conduction band minimum of BiVO₄, which suppresses the photoactivity at longer wavelengths. These findings provide important new insights on the nature of nitrogen incorporation into BiVO₄ and illustrate the need to find alternative lower-bandgap absorber materials for photoelectrochemical energy conversion applications.

1. Introduction

The environmental impact of burning fossil fuels to meet the ever-increasing world energy demand is a primary consideration in the development of future energy systems. The most abundant source of renewable energy is the sun, which provides enough energy to completely replace fossil fuels. However, the intermittency of sunlight (i.e., caused by diurnal and seasonal cycles, weather conditions) necessitates an effective means to store the energy. The conversion of solar energy into chemical energy carriers (i.e., solar fuels) has been recognized as one of the most promising ways to store large amounts of energy for long periods while ensuring compatibility with the current energy infrastructure. One of the simplest and most direct pathways toward solar fuels is photoelectrochemical (PEC) water splitting.^[1] This process produces hydrogen, which can be used either directly as a chemical fuel or as a feedstock for the production of other chemicals (e.g., hydrocarbons, ammonia).

R. Irani, Dr. I. Y. Ahmet, Prof. J.-W. Jang, Dr. S. P. Berglund, Dr. P. Plate, C. Höhn, Dr. P. Bogdanoff, Prof. R. van de Krol, Dr. F. F. Abdi
Institute for Solar Fuels
Helmholtz-Zentrum Berlin für Materialien und Energie GmbH
Hahn-Meitner-Platz 1, Berlin 14109, Germany
E-mail: fatwa.abdi@helmholtz-berlin.de

Dr. R. Böttger
Institute of Ion Beam Physics and Materials Research
Helmholtz-Zentrum Dresden-Rossendorf
Bautzner Landstr. 400, Dresden 01328, Germany

 The ORCID identification number(s) for the author(s) of this article can be found under <https://doi.org/10.1002/solr.201900290>.

© 2019 The Authors. Published by WILEY-VCH Verlag GmbH & Co. KGaA, Weinheim. This is an open access article under the terms of the Creative Commons Attribution License, which permits use, distribution and reproduction in any medium, provided the original work is properly cited.

DOI: 10.1002/solr.201900290

Dr. S. W. Schmitt, Prof. C. Dubourdieu
Institute Functional Oxides for Energy-Efficient Information Technology
Helmholtz-Zentrum Berlin für Materialien und Energie GmbH
Hahn-Meitner-Platz 1, Berlin 14109, Germany

Prof. C. Dubourdieu
Physical Chemistry
Freie Universität Berlin
Arnimallee 22, Berlin 14195, Germany

Dr. S. Lardhi, Prof. L. Cavallo, Dr. M. Harb
KAUST Catalysis Center (KCC)
Physical Sciences and Engineering Division (PSE)
King Abdullah University of Science and Technology (KAUST)
Thuwal 23955-6900, Saudi Arabia

In PEC water splitting systems, semiconducting photoelectrodes are immersed in an aqueous electrolyte. Upon light absorption, charge separation takes place in the bulk of the material, followed by water oxidation/reduction at the surface of the photoelectrodes. For efficient solar water splitting, potential photoelectrode materials should be able to absorb a broad region of the solar spectrum and efficiently transfer the photogenerated electrons and holes to the semiconductor/electrolyte interface to drive the hydrogen and oxygen evolution half-reactions. Metal oxide semiconductors have been of particular interest as photoelectrode materials due to their comparatively good stability in aqueous solutions, abundance of their constituent elements, often favorable band positions for the water oxidation and/or reduction reactions, and the low-cost techniques that can be used to synthesize these materials. In particular, monoclinic scheelite bismuth vanadate (BiVO_4) has attracted widespread attention. It is a moderate bandgap semiconductor ($\approx 2.4\text{--}2.5\text{ eV}$) with suitable band positions for water oxidation and a fairly negative photocurrent onset potential^[2–4]. Recent efforts on identifying the performance limitations and implementing appropriate optimization strategies have resulted in significant improvement of the AM1.5 photocurrent of BiVO_4 ; the highest reported photocurrent already exceeds 90% of the theoretical maximum (based on the bandgap of BiVO_4).^[5] The performance is, therefore, primarily limited by light absorption so that a major photocurrent improvement can only be achieved by reducing the bandgap.

Various empirical methods have been reported to alter the band positions, and thus the bandgap, of metal oxide semiconductors.^[6–9] In the case of BiVO_4 , doping strategies have been extensively explored to alter the charge carrier transport properties, but few attempts have been made to reduce the bandgap by doping or alloying. Photoexcited holes in the valence band have more-than-enough overpotential to oxidize water, whereas the conduction band potential is close to the redox potential for hydrogen evolution $E(\text{H}_2/\text{H}^+)$. Bandgap reduction through modification of the valence band position is, therefore, preferred. This would extend light absorption toward longer wavelengths while maintaining a modest photocurrent onset potential.^[10–14] The valence band edge of BiVO_4 mainly consists of oxygen 2p atomic orbitals with additional contribution from bismuth 6s orbitals.^[15] To shift the valence band upward and decrease the bandgap, oxygen can be substituted with elements whose atomic orbitals are located at higher energies. For example, nitrogen or sulfur can be incorporated into BiVO_4 ; N 2p and S 3p orbitals are expected to narrow the bandgap.^[9,10,16–18] Approaches for reducing the bandgap of BiVO_4 via cation substitution (V substitution with Sb or Bi substitution with Mn or Fe) have also been reported.^[7,19–21]

In this study, we introduce nitrogen into the BiVO_4 lattice using two methods. In the first method, nitrogen was introduced during the deposition procedure by addition of ammonium nitrate to the spray pyrolysis precursor solution (chemical method). In the second method, nitrogen was introduced after the deposition of BiVO_4 via nitrogen ion implantation (physical method). We will show that in both cases nitrogen is present in the form of dinitrogen (N_2) and this enhances the optical absorption at photon energies below 2.4 eV. The PEC response, however, does not improve. By combining the experimental results with density functional theory (DFT) calculations, we show that this can be understood from the changes in the electronic structure of BiVO_4 upon nitrogen incorporation.

2. Results and Discussion

2.1. Structural and Optical Properties

BiVO_4 films deposited by spray pyrolysis are typically annealed in air,^[22] but all the nitrogen-incorporated BiVO_4 films in this study were annealed in pure N_2 to avoid loss of nitrogen during annealing. We therefore first compared the influence of post-deposition annealing in air and N_2 on the structural and optical properties of unmodified BiVO_4 . The X-ray diffraction (XRD) patterns of pristine BiVO_4 samples annealed at 460 °C for 2 h in air and N_2 are shown in Figure S1a, Supporting Information. All XRD peaks could be matched with the standard monoclinic scheelite phase of BiVO_4 (PDF 00-014-0688) and no other phases were found. The optical absorption spectra of both samples are also practically identical, as shown in Figure S1b, Supporting Information. This is different from the report of Kim et al. on N_2 -annealed BiVO_4 ,^[10] in which nanoporous BiVO_4 films synthesized electrochemically showed a shift of the absorption onset upon annealing in N_2 . Clearly, N_2 annealing does not lead to incorporation of nitrogen in our spray-pyrolysed BiVO_4 , despite the higher temperature used in our study (460 °C) as compared with their report (350 °C). We speculate that this is caused by the difference in morphology, crystallinity, and surface chemical properties between the spray-pyrolysed and electrodeposited BiVO_4 ; further study beyond the scope of the current work is needed to unravel the exact cause.

2.1.1. Chemical Incorporation of Nitrogen

Figure 1 shows the XRD patterns for the nitrogen-incorporated BiVO_4 films via the chemical method. For brevity, these films will be designated as N: BiVO_4 (chem.) throughout the remainder of the article. The as-deposited film shows all of the main XRD peaks for the monoclinic scheelite BiVO_4 phase as well as several additional small peaks. Upon post-deposition annealing in N_2 for 2 h at 460 °C, the monoclinic BiVO_4 phase is maintained and two of the additional small peaks remain at 2θ angles of $\approx 27^\circ$ and 28° , which can be assigned to VO_2 (PDF 00-009-0142). We speculate that this is caused by the facile reaction between ammonium and bismuth nitrate, leaving some of the vanadium in the same reduced state as in the precursor (V^{4+} in vanadyl acetylacetonate). The morphologies of the pristine BiVO_4 and N: BiVO_4 (chem.) films, both annealed in N_2 , are shown in Figure 1b,c. The morphology of the N: BiVO_4 (chem.) film is less regular, but the average particle sizes of the pristine BiVO_4 and N: BiVO_4 (chem.) are similar at $0.20 \pm 0.07\ \mu\text{m}$ and $0.18 \pm 0.1\ \mu\text{m}$, respectively. The high-resolution transmission electron microscopy (HR-TEM) image of the N: BiVO_4 (chem.) film shows a clear lattice fringe spacing of 0.36 nm (Figure S2, Supporting Information), which corresponds to the (200) plane of BiVO_4 .^[23]

Tauc analysis was performed to determine the bandgap of the films. **Figure 2** shows the direct and indirect Tauc plots (using the Kubelka–Munk function) for pristine BiVO_4 and N: BiVO_4 (chem.). The direct bandgap is not affected by nitrogen incorporation, but a shift of the indirect bandgap can be observed from $2.55 \pm 0.05\ \text{eV}$ for pristine BiVO_4 to $2.49 \pm 0.05\ \text{eV}$ for N: BiVO_4 (chem.). We note that this small shift is in the same order as the one demonstrated in nitrogen-incorporated BiVO_4

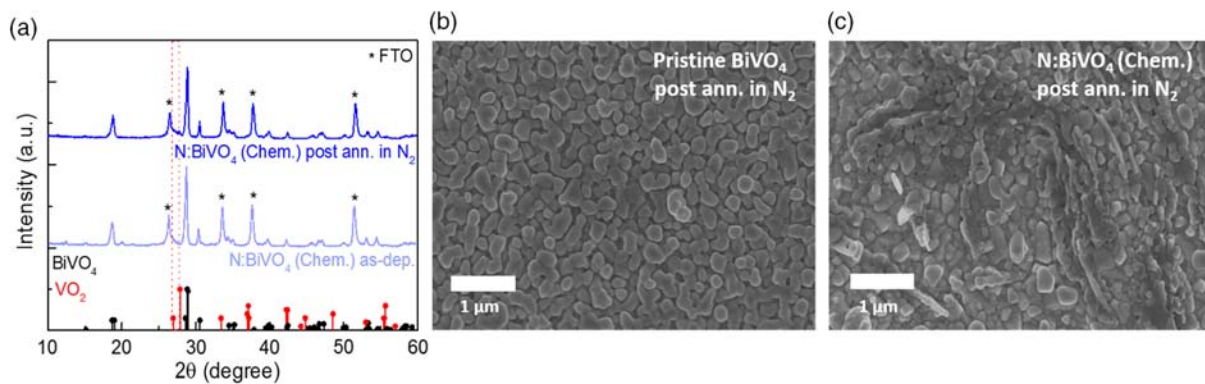


Figure 1. a) XRD pattern of the as-deposited and post-deposition annealed (in N₂ at 460 °C for 2 h) chemically incorporated N:BiVO₄ films. SEM images of b) pristine BiVO₄ and c) N:BiVO₄ (chem.) films. Both films were annealed in N₂ at 460 °C for 2 h.

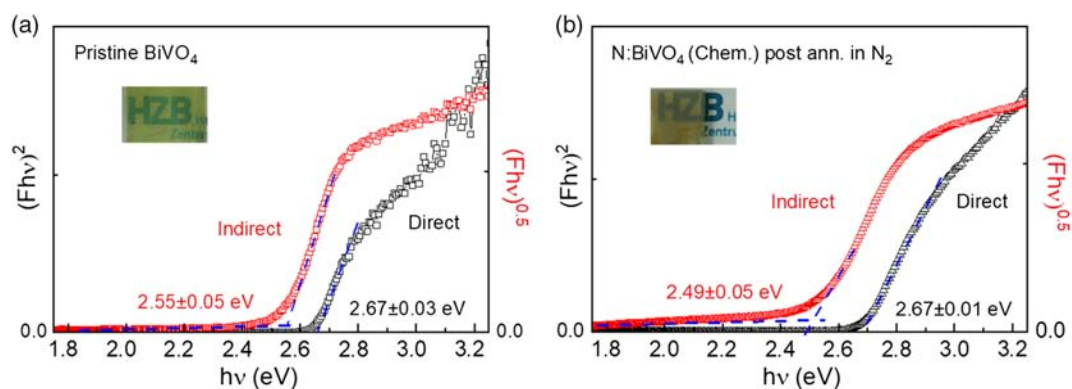


Figure 2. Indirect and direct bandgaps of a) the pristine and b) chemically incorporated nitrogen BiVO₄ samples (all annealed in N₂ at 460 °C for 2 h). Insets show the photographs of the samples.

through N₂ annealing by Kim et al.^[10] Despite the small shift in the indirect bandgap, the N:BiVO₄ (chem.) film was significantly darker (more brown) in visual appearance—see inset of Figure 2 for the photographs of BiVO₄ and N:BiVO₄ (chem.). This may be caused by the absorption tail observed for energies between 1.8 and 2.4 eV (see Figure 2 and Figure S3, Supporting Information). This presumably indicates the presence of defects or disorder, yielding localized states in the bandgap (i.e., Urbach tail).^[24,25]

The optical absorption spectra shown in Figure S3, Supporting Information, also show that the N:BiVO₄ (chem.) films have lower absorbance at wavelengths lower than 500 nm as compared with the pristine films. This is due to the fact that the N:BiVO₄ (chem.) films are thinner (Figure S4, Supporting Information). Although the same amount of precursor was used for the preparation, the addition of ammonium nitrate increases the volatility of the precursor solution during high-temperature spray deposition, which results in a lower deposition rate.

2.1.2. Physical Incorporation of Nitrogen

As an alternative to the chemical incorporation of nitrogen, a physical incorporation approach via nitrogen ion implantation

was also explored. We first simulated the penetration depth and concentration of nitrogen ions inserted to the BiVO₄ lattice as a function of the applied ion energy and fluence using the Stopping and Range of Ions in Matter (SRIM) program. The results obtained from the simulation are shown in Figure 3a,b, respectively. Based on these curves, we prepared nitrogen ion-implanted BiVO₄ films using an ion energy of 40 keV and a fluence of 10¹⁶ cm⁻². This should lead to an N concentration above 10²⁰ cm⁻³ for a depth of up to 150 nm (40 kV data in Figure 3a and 10¹⁶ cm⁻² data in Figure 3b), which corresponds to an average nitrogen-to-bismuth ratio of ≈0.4. For conciseness, these modified films are designated as N:BiVO₄ (phys.). Figure 4a shows the XRD peaks of the N:BiVO₄ (phys.) samples, both as implanted and after post-deposition annealing in N₂. Compared with the pristine sample (Figure S1, Supporting Information), the as-implanted N:BiVO₄ (phys.) has a much lower crystallinity. This is also evident from the scanning electron microscopy (SEM) image (Figure 4b), in which the individual grains are less clearly defined than in pristine BiVO₄ (Figure 1b). Partial amorphization due to damage from high-energy ion implantation has indeed been shown in many reports.^[26,27] Post-deposition annealing of the films in N₂ helps restore the crystallinity (Figure 4a), which is also evident from the SEM micrographs (Figure 4b,c). The morphology of N:BiVO₄ (phys.) consists of elongated particles similar to the pristine

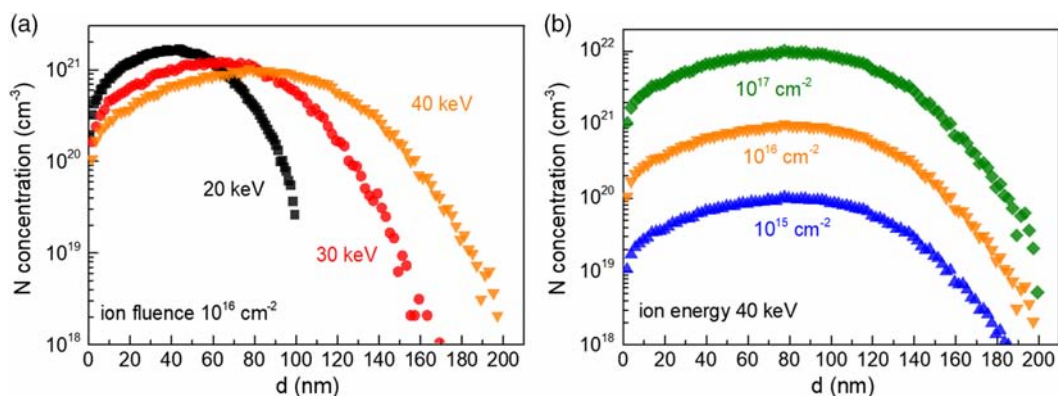


Figure 3. Concentration depth profiles obtained from Monte Carlo simulations using the SRIM program for nitrogen within the BiVO₄ samples for ion implantation at a) a constant ion fluence of 10¹⁶ cm⁻² and varying energies and b) constant ion energy of 40 keV and varying ion fluencies. The x-axis is the depth (*d*) from the surface of the BiVO₄ samples.

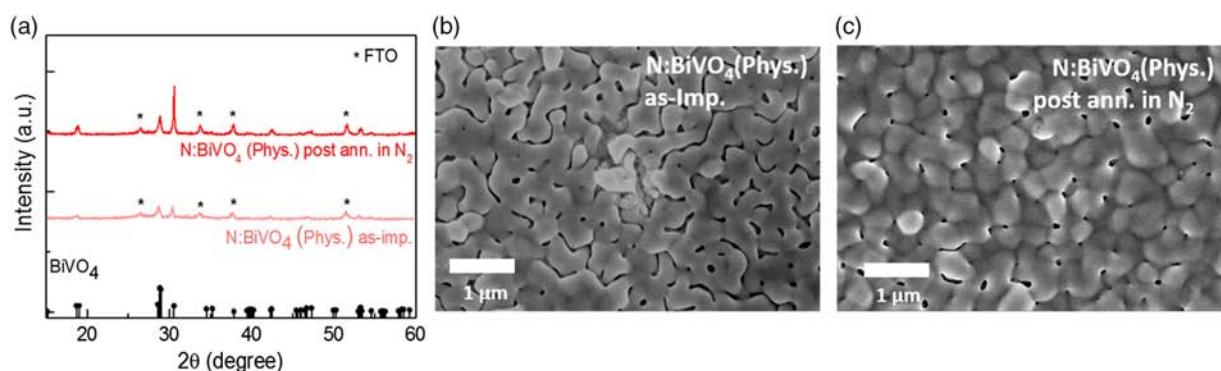


Figure 4. a) XRD patterns of the physically incorporated N:BiVO₄ films, as-implanted and after annealing in N₂ at 460 °C for 2 h. SEM images of b) the as-implanted and c) post-implantation annealed films in N₂ are also shown.

BiVO₄ (Figure 1b), albeit with a larger grain size and less sharply defined grain boundaries. Films with a higher ion fluence (10¹⁷ cm⁻²) were also prepared, but the resulting films show irreversible damage, and post-deposition annealing treatment could not recrystallize the films (Figure S5, Supporting Information).

The absorption spectra of the pristine BiVO₄ and N:BiVO₄ (phys.) films are shown in Figure 5a. The as-implanted N:BiVO₄ (phys.) film shows no distinct absorption features that are typical for monoclinic BiVO₄. This is due to the extensive damage from ion implantation (*vide supra*). Post-implantation annealing in

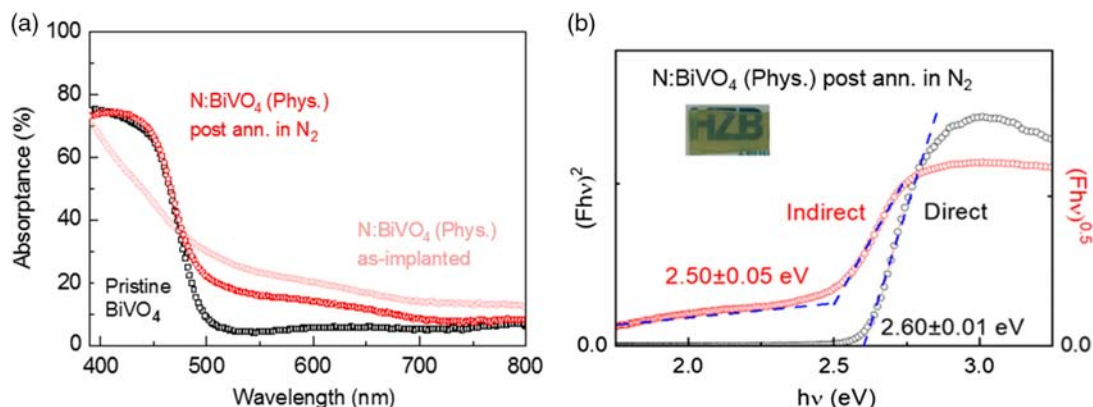


Figure 5. a) Optical absorbance spectra of pristine BiVO₄ and N:BiVO₄ (phys.) films, as implanted and after post-implantation annealing in N₂ (460 °C, 2 h). b) Indirect and direct bandgaps of the physically incorporated N:BiVO₄ sample. The film was annealed at 460 °C in N₂ for 2 h. The inset shows a photograph of the sample.

N_2 successfully brings back the typical monoclinic $BiVO_4$ absorption features, with the addition of an absorption tail that extends up to ≈ 700 nm. This results in a change in the visual appearance of the $N:BiVO_4$ (phys.) films, see the inset of Figure 5. Tauc analysis was performed (Figure 5b), and the indirect bandgap shifts from 2.55 ± 0.05 eV for the pristine $BiVO_4$ to 2.50 ± 0.05 eV for the $N:BiVO_4$ (phys.). The direct bandgap also shifts toward a slightly lower value, from 2.67 ± 0.05 eV in the pristine $BiVO_4$ to 2.60 ± 0.01 eV in $N:BiVO_4$ (phys.).

2.2. Chemical Nature of Incorporated Nitrogen in $N:BiVO_4$ Films

To confirm that the changes in the optical absorption above are truly caused by the incorporation of nitrogen, we performed X-ray photoelectron spectroscopy (XPS) analysis of the pristine $BiVO_4$, $N:BiVO_4$ (chem.), and $N:BiVO_4$ (phys.) films. The N 1s core-level spectra are shown in Figure 6a. Indeed, while the pristine $BiVO_4$ shows no XPS signal for nitrogen (despite the post-deposition annealing in N_2), a clear nitrogen peak at ≈ 400 eV can be observed for both the chemically and physically modified $N:BiVO_4$. Several studies have reported the N 1s XPS spectra in the literature: a peak at 396–398 eV can be assigned to nitrogen at regular lattice sites (nitrogen–metal bonds), whereas a peak at 400–402 eV can be assigned to molecular nitrogen.^[28–31] The lattice and molecular nitrogen peak positions are highlighted by the pink and green regions in Figure 6a, respectively. Based on this, we conclude that nitrogen is present in the molecular form (i.e., as N_2) in our $N:BiVO_4$ films.

We note that our observed peak is slightly different than the one reported by Choi and coworkers in their study on N_2 -annealed

nanostructured $BiVO_4$ samples.^[10] There, a significantly broader peak for nitrogen between 397 and 402 eV was reported. This peak can be assigned to a mixture of mostly molecular N_2 and a small amount of bonding nitrogen that substitutes for lattice oxygen.^[29,30,32] The presence of nitrogen in its molecular form (N_2) seems unusual in a solid-state lattice but has also been reported for, e.g., ZnO ^[33] and WO_3 . Mi et al. reported the trapping of N_2 in the WO_3 lattice in the form of $xN_2 \cdot WO_3$ ($x = 0.034–0.039$), resulting in an extension of the absorption and photoactivity of WO_3 .^[34] The computational results from their study suggested that the red shift in optical absorption is caused by both the deformation of the host lattice (WO_3) and weak electronic interaction between trapped N_2 and the WO_3 matrix.

Bi 4f core-level spectra of the films are shown in Figure 6b. No changes are observed upon the incorporation of nitrogen in $BiVO_4$, for both chemical and physical incorporation. Based on the N 1s and Bi 4f peaks, the N:Bi ratio was estimated to be 0.4 and 0.1 for the $N:BiVO_4$ (chem.) and $N:BiVO_4$ (phys.) films, respectively. For the $N:BiVO_4$ (phys.) film, the N:Bi ratio obtained by XPS is about four times smaller than the estimate obtained from the SRIM simulations (Figure 3). As XPS is a surface-sensitive technique, this discrepancy may be caused by a gradient in nitrogen concentration between the surface and the bulk. Alternatively, some nitrogen may leave the $BiVO_4$ lattice during the post-implantation annealing step. It is nevertheless clear that nitrogen is indeed incorporated in the films and responsible for the observed change in optical absorption. Figure 6c shows the V 2p spectra for the pristine $BiVO_4$, $N:BiVO_4$ (chem.), and $N:BiVO_4$ (phys.) films. From the V 2p peaks, it is clear that the incorporation of nitrogen is accompanied by the formation of V^{4+} , which is consistent with the observation of XRD peaks for VO_2 in Figure 1a.

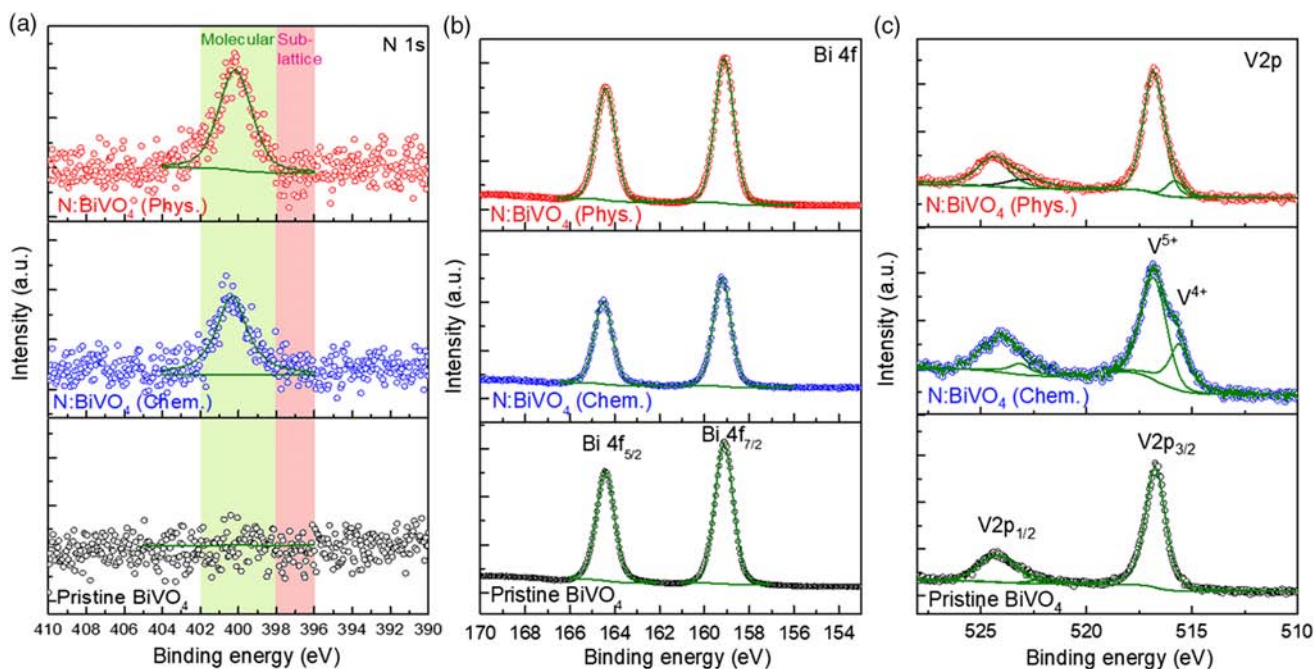


Figure 6. a) N 1s, b) Bi 4f, and c) V 2p core-level XPS spectra of pristine, chemically, and physically nitrogen-incorporated $BiVO_4$. All samples were post-annealed in N_2 at $460^\circ C$ for 2 h.

2.3. Photoelectrochemical Characterization

After successfully introducing nitrogen into the BiVO_4 lattice by both physical and chemical methods, we investigated the photoactivity of our films by measuring their incident photon-to-current conversion efficiency (IPCE). The measurements were performed in a 0.1 M KP_i buffer (pH ≈ 7) with 0.5 M Na_2SO_3 added as a hole scavenger with an applied potential of 1.23 V vs reversible hydrogen electrode (RHE). **Figure 7** shows the IPCE values at different wavelengths for the pristine BiVO_4 , N: BiVO_4 (chem.), and N: BiVO_4 (phys.) films. For the pristine BiVO_4 film, IPCE values of $\approx 60\%$ were obtained for the wavelength range of 350–420 nm. The onset of the IPCE is slightly above 500 nm, which agrees well with the bandgap of BiVO_4 . The N: BiVO_4 (chem.) film shows lower IPCE values, which is attributed to the lower thickness of the film (see Figure S4, Supporting Information). Multiplication of the IPCE spectrum of the N: BiVO_4 (chem.) film with a factor of ≈ 1.5 results in an almost overlapping spectrum with that of the pristine BiVO_4 film (inset, Figure 7) and shows no sign of a shift in absorption onset. Finally, the as-implanted N: BiVO_4 (phys.) film shows no photoactivity (i.e., zero IPCE) for all wavelength ranges due to

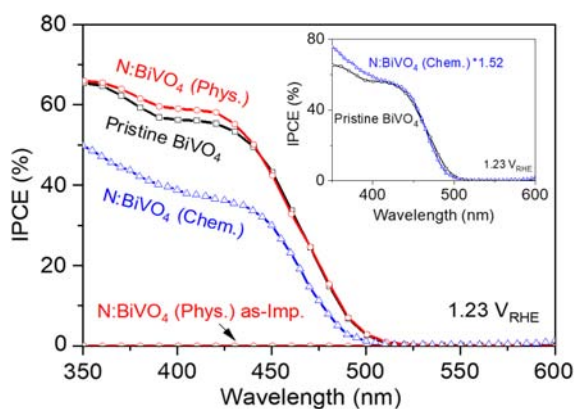


Figure 7. Incident photon-to-current conversion efficiency (IPCE) versus wavelength curves of pristine BiVO_4 , chemically, and physically prepared N: BiVO_4 samples. The measurements were done at 1.23 V vs RHE in 0.1 M potassium phosphate buffer (pH ≈ 7) with 0.5 M of sodium sulfite electrolyte. The inset shows no change in the IPCE onset for the N: BiVO_4 (chem.) sample. All samples were annealed in N_2 at 460 °C for 2 h, except for the as-implanted physically prepared samples that were not photoactive.

the poor crystallinity caused by ion beam damage. After annealing in nitrogen, the IPCE spectrum of the N: BiVO_4 (phys.) film overlaps with that of the pristine BiVO_4 film; no shift of the onset of the IPCE was observed. This shows that post-implantation annealing not only improves the crystallinity but also recovers the photoactivity. An XPS measurement of the film after the PEC measurement reveals that nitrogen is still present in N: BiVO_4 (Figure S6, Supporting Information). The AM1.5 photocurrents of the samples show no significant difference—except for the thickness-related effect of the N: BiVO_4 (chem.) sample, as also observed in the IPCE—and no shift of the onset potential is observed with the incorporation of nitrogen (Figure S7, Supporting Information). Overall, our measurements revealed that there is no change in the IPCE onset for the films prepared by both techniques, despite clear evidence that nitrogen is present in the films. The exact cause of this is discussed in the next section.

2.4. Density Functional Theory Calculation

To confirm and further explain the experimental results earlier, DFT analysis was performed. We first investigated the likelihood of nitrogen incorporation into BiVO_4 in the molecular form (i.e., N_2) from the thermodynamic point of view. One N_2 molecule was inserted into the $2 \times 1 \times 2$ monoclinic supercell structural model containing 16 Bi, 16 V, and 64 O atoms (see **Figure 8**) to obtain a N:Bi ratio of ≈ 0.1 , mimicking the obtained experimental results. Various possible N_2 structural configurations inside the BiVO_4 lattice were explored covering different orientations and coordination numbers. The configurations converged after full optimization to only three distinct but energetically degenerate structures (i.e., the same lowest electronic energy). This indicates the feasibility of N_2 incorporation in different positions inside the lattice. The relaxed structures revealed the three main N_2 coordination environments that can exist: bridging between 1) two V sites (Figure 8b), 2) two Bi sites (Figure 8c), or 3) one Bi site and one V site (Figure 8d).

As the three configurations of N: BiVO_4 earlier are energetically degenerate, the thermodynamic stability was investigated only for one configuration, which is the one where N_2 bridges between two V atoms. Each N is coordinated to the nearest V located in a VO_4 tetrahedral environment with a N–V distance of 2.27 Å and a constant N–N bond length of 1.13 Å. The computed lattice parameters indicated a minimal distortion of N: BiVO_4 as compared with the

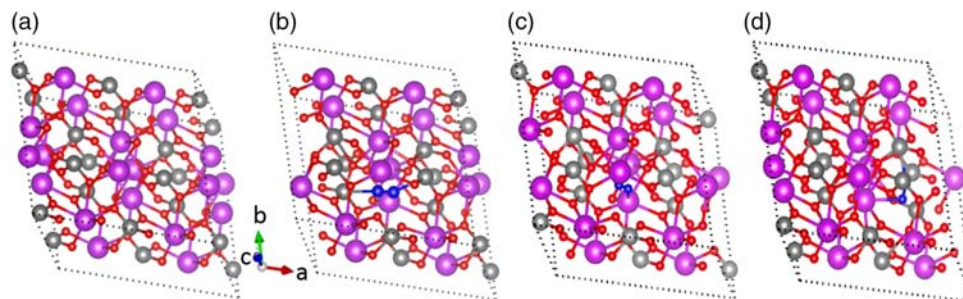


Figure 8. Optimized ball and stick model structure of a) pristine BiVO_4 and N: BiVO_4 ($\text{BiVO}_4\text{N}_{0.125}$) with incorporated N_2 bridging between b) two V, c) two Bi, and d) one V and one Bi. Magenta: Bi, gray: V, red: O, blue: N. An unobstructed view of the N_2 coordination in (b–d) is shown in Figure S8, Supporting Information (reduced stick model).

pristine material (Table S1, Supporting Information). This implies that the incorporation of the N_2 molecule in the $BiVO_4$ lattice does not break the lattice symmetry, nor does it change the position of the neighboring atoms. The thermodynamic stability of $N:BiVO_4$ was studied through DFT calculations using molecular nitrogen N_2 in the gas phase as a nitrogen source and following the experimental conditions. The thermodynamic diagram shown in Figure 9 was built by plotting the formation energy of $N:BiVO_4$ as a function of the nitrogen chemical potential ($\Delta\mu_N$), which represents a more or less oxidizing environment. The $N:BiVO_4$ structure is thermodynamically less stable than $BiVO_4$ at low N_2

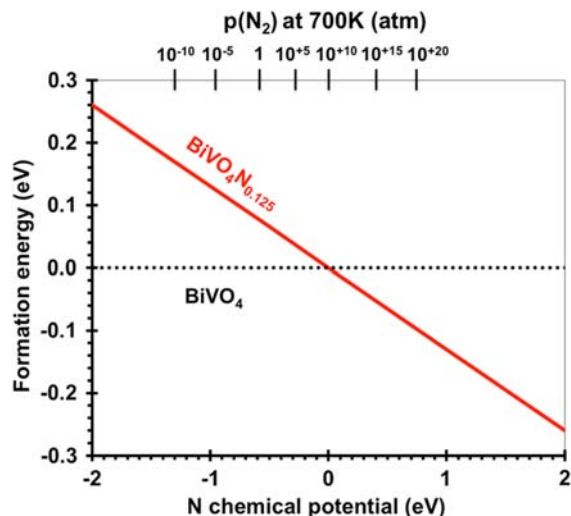


Figure 9. DFT-based formation energy of $BiVO_4N_{0.125}$ (solid red line) as a function of $\Delta\mu_N$ using dinitrogen (N_2) in gas phase as the N source at $T = 700$ K. The dashed black line (zero formation energy) represents the pristine $BiVO_4$.

pressure (under N -poor conditions), whereas it becomes competitive with $BiVO_4$ under standard conditions (i.e., formation energy < 0.1 eV near N_2 atmospheric pressure) and more stable at high N_2 pressure (under N -rich conditions). This shows that it is indeed not surprising that molecular nitrogen can be introduced in the $BiVO_4$ lattice under N -rich experimental conditions (physical/chemical incorporation followed by annealing in pure N_2 atmosphere).

Electronic density of states (DOS) calculations for the various configurations were performed to determine the most likely configuration of molecular nitrogen in $BiVO_4$; the results are shown in Figure 10. Note that the absolute value of the bandgap of $BiVO_4$ is overestimated using our calculation method (see 4 Experimental Section), but we focus on the relative differences between the various configurations in this study. In all cases, the electronic behaviors of the valence band and conduction band states are similar, except for the configuration where the N_2 bridges between two V atoms (Figure 10b). For this configuration, a new empty electronic state appears at ≈ 0.1 eV below the original conduction band minimum (CBM). This leads to a narrower bandgap of $N:BiVO_4$ by ≈ 0.1 eV (see Figure 10b) and consequently a slight shift of the onset of the dielectric function to lower energy by the same amount (see Figure S9, Supporting Information) as compared with the pristine material. This is in a good agreement with the bandgap shift observed in our experiments (Figure 2 and 5). The two other possible structural configurations obtained for $N:BiVO_4$ (incorporated N_2 bridging between two Bi sites or between one Bi and one V site) did not show any change in the bandgap with respect to the pristine material (see Figure 1c,d). Raman spectroscopy of the $N:BiVO_4$ (chem.) sample (Figure S10, Supporting Information) indeed shows the presence of the V–N bond^[35] and the absence of a Bi–N bond, in agreement with the configuration in which N_2 bridges between two V atoms. To further confirm this, the 3D electron density maps of the valence and conduction band

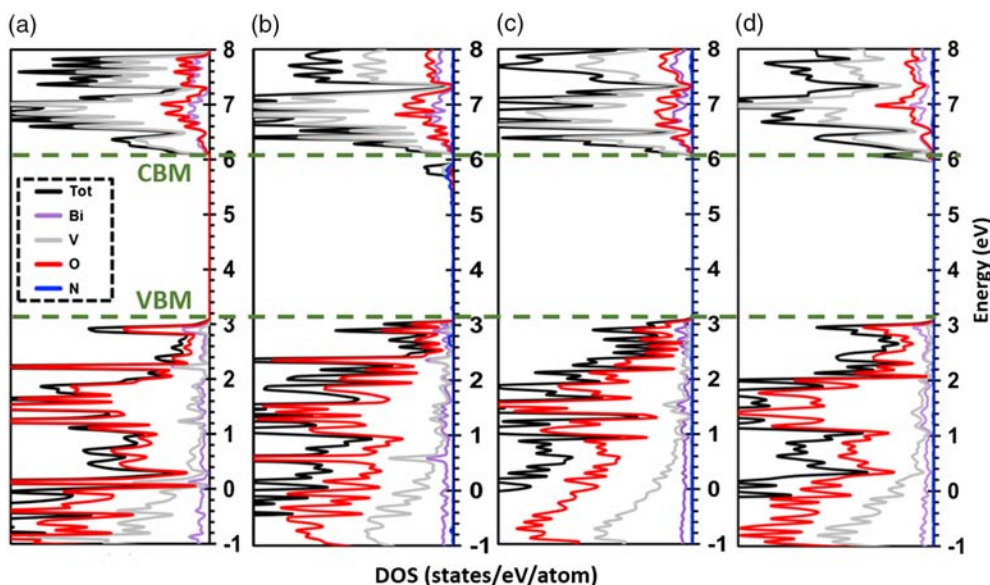


Figure 10. Total/partial electronic DOS obtained using the HSE06 functional for a) pristine $BiVO_4$ and $N:BiVO_4$ with different configurations: N_2 bridging between b) two V sites (see Figure 9b), c) two Bi sites (see Figure 9c), or d) one Bi site and one V site (see Figure 9d). Color legend: total DOS in black; DOSs projected onto Bi 6s orbitals in purple, onto V 3d orbitals in grey, onto O 2p orbitals in red, and onto N 2p orbitals in blue.

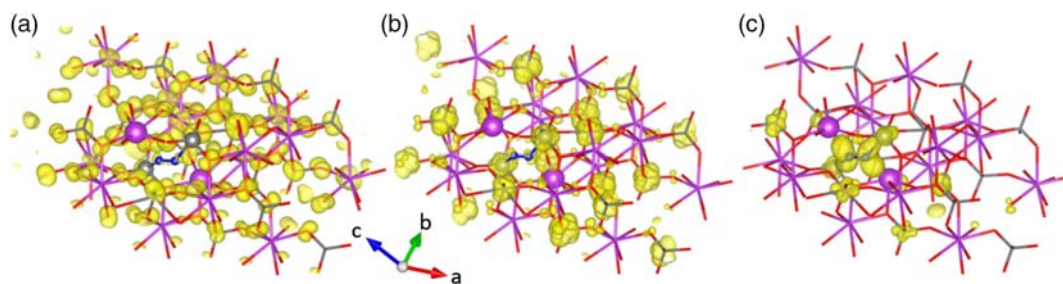


Figure 11. Electron density maps for a) the VBM, b) the CBM, and c) the new generated empty state obtained at the DFT/HSE06 level for the most relevant predicted $\text{BiVO}_4\text{N}_{0.125}$ with incorporated N_2 bridging between two V sites. Color legend: Bi in purple, V in gray, O in red, and N in blue. Sticks represent the bond between atoms. N atoms and their vanadium bridging neighbors are shown with balls. Isovalue is 0.003 au.

electronic states of $\text{N}:\text{BiVO}_4$ (with N_2 bridging between two V sites) were computed and are shown in **Figure 11**. The valence band maximum (VBM) is predominantly composed of a strong contribution of oxygen p-orbitals distributed homogeneously throughout the lattice along with weak contributions from bismuth s-orbitals and vanadium d-orbitals (see Figure 11a). The CBM mainly consists of a major contribution of d-orbitals localized on V distributed homogeneously throughout the crystal lattice together with minor contributions from O 2p-orbitals and Bi p-orbitals (see Figure 11b). This interpretation is consistent with previous DFT reports.^[2,36] The rather delocalized character of the VBM and CBM electronic states is expected to lead to a good migration of the photogenerated holes and electrons to the surface. For the newly generated empty state (≈ 0.1 eV below CBM), however, the electron is localized mainly on the incorporated N_2 and the two linked reduced V species (see Figure 11c). This state may act as an effective electron trap and/or recombination center, which explains the absence of a sub-bandgap photoresponse in the IPCE spectrum. All of these computed results are in good agreement with the experimental observations, and we conclude that the incorporated N_2 most likely bridges between two V atoms (Figure 8b) in our experimentally obtained $\text{N}:\text{BiVO}_4$ samples.

3. Conclusion

In summary, two different approaches of nitrogen incorporation in BiVO_4 thin films have been investigated. The first is via the modification of the spray pyrolysis precursor solution (chemical method) and the second is through nitrogen ion implantation (physical method). The high-energy ion-implantation process damages the crystal structure of the film, but it can be restored with a simple post-implantation annealing in a nitrogen environment. Both the chemical and physical methods lead to a darker appearance of the BiVO_4 films, and UV-Vis analysis shows a slight reduction in the bandgap and the presence of an absorption tail up to ≈ 700 nm. XPS data confirm that nitrogen is indeed incorporated in the BiVO_4 lattice. The position of the N 1s peak suggests that nitrogen is present in the molecular form (i.e., N_2), and thermodynamic DFT calculations confirm the structural likelihood of this configuration. Molecular nitrogen is bonded with two vanadium atoms in the lattice, which introduces a new empty state ≈ 0.1 eV below the CBM. The localized nature of this state suggests that it may act as an electron trap and/or recombination center, which would suppress the photoactivity. Indeed, our

incident photon-to-current conversion efficiency (IPCE) measurement shows no sub-bandgap photoresponse upon nitrogen incorporation with both chemical and physical methods. Although not shown in this article, other methods of incorporating nitrogen into our spray-deposited BiVO_4 thin film (e.g., high-temperature annealing in NH_3 , N_2 plasma treatment) also result in no extension in the spectral range of photoactivity. Therefore, other strategies to reduce the bandgap of BiVO_4 (e.g., incorporation of other elements such as sulfur,^[16] antimony,^[20] or selenium^[37]), which also effectively extend the onset of photoactivity, need to be explored further, for example, with combinatorial and high-throughput methodologies.^[38,39] Alternatively, novel complex metal oxides with similar properties to BiVO_4 , but a smaller bandgap (ideally 1.8–1.9 eV) need to be developed.

4. Experimental Section

Deposition of BiVO_4 Thin-Film Photoanodes: BiVO_4 thin films were deposited on commercial fluorine-doped tin oxide (FTO)-coated glass substrates ($15 \Omega \square^{-1}$, TEC-15, Pilkington) using a low-cost and facile spray pyrolysis technique.^[16,22,40,41] Substrates were cleaned by three successive ultrasonication steps in 10 vol% Triton X-100 solution (Sigma-Aldrich), acetone, and ethanol, each for 15 min. The precursor solution was prepared by dissolving $\text{Bi}(\text{NO}_3)_3 \cdot 5\text{H}_2\text{O}$ (98%, Alfa Aesar) in acetic acid (99.8%, Sigma-Aldrich) and absolute ethanol (VWR Chemicals), whereas $\text{VO}(\text{AcAc})_2$ (99%, Acros Organics) was dissolved separately in absolute ethanol. The amount of Bi and V precursors was adjusted so that each concentration in the final solution was 4 mM, and the ratio of the acetic acid and absolute ethanol in the final 100 mL solution was 1:9. The solutions were ultrasonicated for 15 min separately, mixed subsequently, and finally ultrasonicated again for 15 min. The solution was sprayed using a Quickmist air-atomizing spray nozzle (1/4QM)AU-NC + SUQR-200) onto the substrates, which were placed on a hot plate. The distance between the spray nozzle and the hot plate was 20 cm. A pulsed spray mode was used: 5 s spray followed by 53 s delay to allow for solvent evaporation. To deposit each film, 100 or 200 cycles were applied, and the deposition rate was ≈ 1 nm per cycle. The hot plate temperature was kept constant at 450°C during deposition. Prior to the deposition of BiVO_4 , a thin interfacial layer of SnO_2 (5 mL solution of 0.1 M SnCl_4 [98%, Aldrich] in ethyl acetate [99.8%, VWR Chemical]) was first deposited as a hole-blocking layer^[42] on the FTO substrates at 425°C using the same pulsed spray mode. An unmodified reference sample was prepared by post-deposition annealing of the BiVO_4 film in air at 460°C for 2 h. As all the nitrogen-incorporated samples were post-annealed in N_2 , a control BiVO_4 sample was also prepared by post-deposition annealing in pure N_2 at 460°C for 2 h.

Nitrogen Incorporation into BiVO_4 : Chemical Method. For nitrogen incorporation by the chemical method, NH_4NO_3 (95%, Alfa Aesar) was dissolved in 20 mL of ethanol and added into the BiVO_4 precursor solution described earlier. Various concentrations (16, 32, 40 mM) were

used, but due to the volatility of the precursor upon decomposition the amount of nitrogen in the deposited BiVO₄ film differs from the amount in the precursor solution. To prevent premature hydrolysis of NH₄NO₃, 40 μL and 2 mL of triethyl orthoformate (TEOF, 98% Merck) were also added to the Bi and V precursor solutions, respectively. This step was not done for the standard BiVO₄ deposition because no NH₄NO₃ was added. Finally, the as-deposited films were annealed in pure N₂ at 460 °C for 2 h.

Nitrogen Incorporation into BiVO₄: Physical Method. For nitrogen incorporation by the physical method, N⁺ ion implantation was done at the Ion Beam Center (IBC) within the Helmholtz-Zentrum Dresden-Rossendorf. The ion implantation was conducted at room temperature with ion energies between 20 and 40 keV and ion fluences between 10¹⁵ and 10¹⁷ cm⁻². The penetration depth of the nitrogen ions in the BiVO₄ thin-film samples, at various ion energies and fluencies, was estimated from Monte Carlo simulations using the SRIM program.^[43] A value of 6.1 g cm⁻³ was used as the density of BiVO₄.^[44] To improve the crystallinity of the films after the ion implantation process, they were annealed at 460 °C in pure N₂ for 2 h.

Nitrogen Incorporation into BiVO₄: Material Characterization. A Bruker D8 diffractometer with Cu Kα radiation at 40 kV and 40 mA was used for XRD measurements. SEM images were taken using a LEO GEMINI 1530. UV-Vis measurements were conducted using a PerkinElmer Lambda 950 spectrophotometer equipped with an integrating sphere. To measure transmittance (the sum of transmittance and reflectance), the films were placed inside the integrating sphere with a center mount sample holder positioned at a ≈7.5° offset from the incident light. As some films showed a certain degree of scattering, the Kubelka–Munk function (*F*) was used to determine the absorption.^[17,45] The Kubelka–Munk function is given by Equation (1)

$$F = \frac{(1 - TR)^2}{2TR} \quad (1)$$

where TR is the transmittance of the film. The bandgap was then determined from Tauc analysis, by plotting the value of $(Fh\nu)^n$ ($n = 0.5$ and 2 for indirect and direct transitions, respectively) versus the incident photon energy ($h\nu$) and extrapolating the linear part of the plot to the baseline. XPS measurements (SPECS PHOIBOS 100) were performed using monochromatic Al Kα radiation ($h\nu = 1486.74$ eV, SPECS FOCUS 500 monochromator). The pass energy was set to 30 and 10 eV with step sizes of 0.5 and 0.05 eV for the survey and fine spectra, respectively. The binding energies were calibrated with the adventitious carbon C1s peak at 284.5 eV. Fitting of the peaks was done using XPSPEAK software, and a Shirley background subtraction was done for all spectra. For Raman measurements, a HORIBA LabRam HR Evolution spectrometer was used for backscattering configuration, equipped with a 325 nm continuous wave (CW) laser source. Excitation and signal collection were performed via a 40 × NUV objective and the acquired Raman spectra were analyzed with a silicon charge-coupled device (CCD) camera with 1800 lines mm⁻¹ grating blazed at 400 nm. Measurements were executed at an incident power of 1 mW with an integration time of 2 × 120 s. Raman spectra were smoothed by adjacent averaging of 7 points (1 point = 1.5 cm⁻¹). A background correction was further applied to remove an underlying broadband photoluminescence emission which the samples showed upon excitation with the blue laser at 325 nm. Transmission electron microscopy (TEM) was performed using a Philips CM12. The applied acceleration voltage was kept constant at 120 kV. For high resolution, LaB6 cathode and Super TWIN lens were used (0.30 nm point and 0.14 nm line resolution). The camera was a 2k × 2k CCD from Gatan (Orius SC 830).

Nitrogen Incorporation into BiVO₄: Photoelectrochemical Characterization. PEC measurements were performed in a three-electrode configuration using a custom Teflon cell.^[1] The electrolyte was 0.1 M potassium phosphate buffer (KP_i, pH ≈ 7) prepared by mixing 8.21 g of potassium phosphate monobasic (KH₂PO₄, 99.5%, Merck) and 8.67 g of potassium hydrogen phosphate trihydrate (K₂HPO₄·3H₂O, 99%, Merck) in 1 L of Milli-Q water (18.2 MΩ cm). 0.5 M of sodium sulfite (Na₂SO₃, 99%, Merck) was added as a hole scavenger. The potential of the working electrode (i.e., BiVO₄ or N:BiVO₄ samples) was controlled by a potentiostat (EG&G 283, Princeton Applied Research). A Pt wire was the counter electrode, and an

Ag/AgCl electrode (XR300, saturated KCl solution, Radiometer Analytical) was used as the reference electrode. Potentials with respect to Ag/AgCl potential were converted into the RHE scale using Nernst equation

$$V_{\text{RHE}} = V_{\text{Ag/AgCl}} + 0.0591 \times \text{pH} + V_{\text{Ag/AgCl}}^0 \quad (2)$$

where $V_{\text{Ag/AgCl}}^0$ is the standard potential of the Ag/AgCl reference electrode (0.199 V at 25 °C). Monochromatic back-side illumination (i.e., light arriving from the substrate side) was provided by coupling a Xe lamp (LOT, LSH302) with an Acton Research monochromator (SP2150) and long-pass filters (3 mm thick, Schott). The intensity of the monochromatic light was measured using a calibrated photodiode (PD300R-UV diode read by a Nova II controller, Ophir). The following equation was applied to calculate the incident photon-to-current conversion efficiency (IPCE) values

$$\text{IPCE}(\lambda)(\%) = \frac{1240(\text{V nm}) \times J_p(\lambda)(\text{mA/cm}^2)}{\lambda(\text{nm}) \times I_\lambda(\lambda)(\text{mW/cm}^2)} \times 100 \quad (3)$$

where $J_p(\lambda)$ is the measured photocurrent density and $I_\lambda(\lambda)$ is the incident light power density for each wavelength (λ).

Nitrogen Incorporation into BiVO₄: DFT Calculation. The clinobisvanite phase of BiVO₄ (C_{2/c} space group) is modeled by a 2 × 1 × 2 supercell containing 16 functional units (Bi₁₆V₁₆O₆₄) or 96 atoms. For N:BiVO₄, based on experimental XPS measurements revealing a N:Bi ratio of around 0.1, one neutral molecule of nitrogen (N₂) was inserted into the lattice. Several possibilities of N₂ incorporation were investigated based on the type and number of bonded species to the N₂ dimer. One group of configurations consisted of N₂ bridging between two Bi sites, two V sites, or one Bi site and one V site from the same layer. The other group consisted of bridging N₂ to two Bi sites, two V sites, or one Bi site and one V site from two adjacent layers. Other insertion sites were neglected, as they are equivalent due to the high-symmetry lattice of BiVO₄.

Pristine and N:BiVO₄ structures were optimized using the periodic DFT, as implemented in the Vienna Ab initio simulation package (VASP) program,^[46,47] along with the Perdew–Burke–Ernzerhof (PBE) exchange-correlation functional^[48] and the projected-augmented plane-wave (PAW) approach^[49]. The valence electron configurations adopted in the PAW potentials were 6s²6p³ for Bi, 3p⁶3d⁴4s¹ for V, 2s²2p⁴ for O, and 2s²2p³ for N. The kinetic cut-off energy for the plane-wave expansion and charge augmentation was set to 400 eV. The atomic positions and cell parameters were fully relaxed so that the Hellmann–Feynman forces on the atoms, the stress on the cell, and the energy change per atom were less than 0.01 eV Å⁻¹, 0.02 GPa, and 1 × 10⁻⁵ eV, respectively. The size of the Monkhorst–Pack *k*-point mesh^[50] for sampling the Brillouin zone was set to 3 × 3 × 3. Thermodynamic stability calculations were applied to the optimized structures by mimicking the experimental condition adopted for synthesis. The considered reaction used the dinitrogen N₂ in the gas phase as an incorporation agent as follows



Following this, the formation energy was calculated using the following expression

$$E_{\text{form}}(1) = E_{\text{tot}}[\text{BiVO}_4\text{N}_x] - E_{\text{tot}}[\text{BiVO}_4] - \frac{x}{2} \cdot E_{\text{tot}}[\text{N}_2] - x \cdot \Delta\mu_{\text{N}} \quad (5)$$

The total energies of BiVO₄ and N:BiVO₄ materials in their lowest-energy configuration were described by $E_{\text{tot}}[\text{BiVO}_4]$ and $E_{\text{tot}}[\text{BiVO}_4\text{N}_x]$ where $x = 0.125$. $E_{\text{tot}}[\text{N}_2]$ represents the total energy of N₂ molecule in the gas phase. The thermal part of the nitrogen chemical potential ($\Delta\mu_{\text{N}}$) depends on temperature (*T*) and partial pressure (*p*) through the enthalpy (*h*) and entropy (*s*) corrections as described in the following equation

$$\Delta\mu_{\text{N}} = h_{\text{N}_2}(T) - T \cdot s_{\text{N}_2}(T) + \text{RT} \ln \left[\frac{p(\text{N}_2)}{p_0} \right] \quad (6)$$

The zero-point vibrational energy as a function of *T* and *p* was included into the thermal corrections of N₂. It was computed with the DMol

program^[51] using the PBE exchange-correlation functional and the double numerical basis set with polarization (DNP)^[52]. Here, $\Delta\mu_N$ was varied as a function of $p(N_2)$ at $T = 700$ K, which is close to the experimental conditions. For pristine BiVO₄, the reference formation energy was set to 0 eV to compare the relative stability of the N:BiVO₄ material. This approach has been proven to be successful in matching the experimental observations while investigating the thermodynamic stability of H-doped BiVO₄^[53] and S-doped BiVO₄^[16] materials used in photocatalysis and photoelectrochemistry.

The electronic structure calculations of these materials were conducted using DFT using the screened coulomb hybrid Heyd–Scuseria–Ernzerhof (HSE06) exchange-correlation functional,^[54–56] as implemented in VASP, based on the optimized geometries obtained at the PBE level. The tetrahedron method with Blöchl corrections was used for Brillouin-zone integration. HSE06 functional is used here to overcome the well-known limitation of generalized gradient approximation (GGA) functional as it underestimates the experimental bandgap values.^[57–59] It is worth mentioning that the focus in this study is on the relative shift rather than the absolute value of the bandgap. Optical absorption calculations of those structures were conducted by applying the sum-over-empty states (SOS) method as implemented in VASP along with HSE06. Simulated optical absorption spectra were deduced from the imaginary part of the frequency-dependent complex dielectric function, taking into account the summation of all possible electronic transitions from occupied to empty levels and calibrated by the momentum matrix elements, giving the probability of each transition.^[60]

Supporting Information

Supporting Information is available from the Wiley Online Library or from the author.

Acknowledgements

This research was supported by the German Federal Ministry of Education and Research (BMBF), project “MANGAN” (03SF0505), and Europe’s Fuel Cell and Hydrogen Joint Undertaking (FCH-JU), project “PECDEMO” (Grant Agreement no. 621252). Parts of this research were conducted at IBC at Helmholtz-Zentrum Dresden-Rossendorf e.V., a member of the Helmholtz Association. For computational resources, this research used the Shaheen II supercomputer of KAUST Supercomputing Laboratory in Thuwal, Saudi Arabia.

Conflict of Interest

The authors declare no conflict of interest.

Keywords

bandgaps, BiVO₄, molecular nitrogen, photoanode, photoelectrochemistry

Received: June 27, 2019

Revised: September 2, 2019

Published online: October 1, 2019

- [1] R. van de Krol, M. Grätzel, *Photoelectrochemical Hydrogen Production*, Springer, New York, NY, USA **2012**.
 [2] J. K. Cooper, S. Gul, F. M. Toma, L. Chen, P.-A. Glans, J. Guo, J. W. Ager, J. Yano, I. D. Sharp, *Chem. Mater.* **2014**, *26*, 5365.
 [3] J. K. Cooper, S. Gul, F. M. Toma, L. Chen, Y.-S. Liu, J. Guo, J. W. Ager, J. Yano, I. D. Sharp, *J. Phys. Chem. C* **2015**, *119*, 2969.

- [4] L. Gao, F. Li, H. Hu, X. Long, N. Xu, Y. Hu, S. Wei, C. Wang, J. Ma, J. Jin, *ChemSusChem* **2018**, *11*, 2502.
 [5] Y. Pihosh, I. Turkevych, K. Mawatari, J. Uemura, Y. Kazoe, S. Kosar, K. Makita, T. Sugaya, T. Matsui, D. Fujita, M. Tosa, M. Kondo, T. Kitamori, *Sci. Rep.* **2015**, *5*, 11141.
 [6] C.-Z. Ning, L. Dou, P. Yang, *Nat. Rev. Mater.* **2017**, *2*, 17070.
 [7] M. R. Dolgos, A. M. Paraskos, M. W. Stoltzfus, S. C. Yarnell, P. M. Woodward, *J. Solid State Chem.* **2009**, *182*, 1964.
 [8] R. Liu, J. Ren, D. Zhao, J. Ning, Z. Zhang, Y. Wang, Y. Zhong, C. Zheng, Y. Hu, *Inorg. Chem. Front.* **2017**, *4*, 2045.
 [9] R. M. Navarro Yerga, M. C. Álvarez Galván, F. del Valle, J. A. Villoria de la Mano, J. L. G. Fierro, *ChemSusChem* **2009**, *2*, 471.
 [10] T. W. Kim, Y. Ping, G. A. Galli, K.-S. Choi, *Nat. Commun.* **2015**, *6*, 8769.
 [11] J. Zeitouny, E. A. Katz, A. Dollet, A. Vossier, *Sci. Rep.* **2017**, *7*, 1766.
 [12] D. B. Khadka, J. Kim, *J. Phys. Chem. C* **2015**, *119*, 1706.
 [13] X. Zhu, X. Luo, H. Yuan, H. Chen, C. Tian, *RSC Adv.* **2018**, *8*, 3304.
 [14] W. J. Jo, H. J. Kang, K.-J. Kong, Y. S. Lee, H. Park, Y. Lee, T. Buonassisi, K. K. Gleason, J. S. Lee *Proc. Natl. Acad. Sci.* **2015**, Vol. 112, p. 13774.
 [15] M. Oshikiri, M. Boero, J. Ye, Z. Zou, G. Kido, *J. Chem. Phys.* **2002**, *117*, 7313.
 [16] M. Lamers, W. Li, M. Favaro, D. E. Starr, D. Friedrich, S. Lardhi, L. Cavallo, M. Harb, R. van de Krol, L. H. Wong, F. F. Abdi, *Chem. Mater.* **2018**, *30*, 8630.
 [17] H. Fakhouri, J. Pulpytel, W. Smith, A. Zolfaghari, H. R. Mortaheb, F. Meshkini, R. Jafari, E. Sutter, F. Arefi-Khonsari, *Appl. Catal. B* **2014**, *144*, 12.
 [18] W. Smith, H. Fakhouri, J. Pulpytel, S. Mori, R. Grilli, M. A. Baker, F. Arefi-Khonsari, *J. Phys. Chem. C* **2012**, *116*, 15855.
 [19] M. Zhang, Y. Ma, D. Friedrich, R. van de Krol, L. H. Wong, F. F. Abdi, *J. Mater. Chem. A* **2018**, *6*, 548.
 [20] A. Louidice, J. Ma, W. S. Drisdell, T. M. Mattox, J. K. Cooper, T. Thao, C. Giannini, J. Yano, L.-W. Wang, I. D. Sharp, R. Buonsanti, *Adv. Mater.* **2015**, *27*, 6733.
 [21] Z. Jiao, J. Zheng, C. Feng, Z. Wang, X. Wang, G. Lu, Y. Bi, *ChemSusChem* **2016**, *9*, 2824.
 [22] M. Lamers, S. Fiechter, D. Friedrich, F. F. Abdi, R. van de Krol, *J. Mater. Chem. A* **2018**, *6*, 18694.
 [23] T. Palaniselvam, L. Shi, G. Mettela, D. H. Anjum, R. Li, K. P. Katuri, P. E. Saikaly, P. Wang, *Adv. Mater. Interfaces* **2017**, *4*, 1700540.
 [24] S. Pimputkar, S. Suihkonen, M. Imade, Y. Mori, J. S. Speck, S. Nakamura, *J. Cryst. Growth* **2015**, *432*, 49.
 [25] A. S. Hassanien, A. A. Akl, *J. Alloys Compd.* **2015**, *648*, 280.
 [26] A. Macková, P. Malinský, A. Jágerová, Z. Sofer, D. Sedmidubský, K. Klímová, R. Böttger, S. Akhmedaliev, *Surf. Interface Anal.* **2018**, *50*, 1099.
 [27] K. Lorenz, M. Peres, N. Franco, J. G. Marques, S. M. C. Miranda, S. Magalhães, T. Monteiro, W. Wesch, E. Alves, E. Wendler, in *Proc. SPIE 2011*, *7940*, p. 79400O.
 [28] R. Asahi, T. Morikawa, T. Ohwaki, K. Aoki, Y. Taga, *Science* **2001**, *293*, 269.
 [29] C. S. Kang, H.-J. Cho, K. Onishi, R. Nish, R. Choi, S. Gopalan, S. Krishnan, J. H. Han, J. C. Lee, *Appl. Phys. Lett.* **2002**, *81*, 2593.
 [30] W. F. Egelhoff, *Surf. Sci. Lett.* **1984**, *141*, L324.
 [31] J. Wang, D. N. Tafen, J. P. Lewis, Z. Hong, A. Manivannan, M. Zhi, M. Li, N. Wu, *J. Am. Chem. Soc.* **2009**, *131*, 12290.
 [32] N. C. Saha, H. G. Tompkins, *J. Appl. Phys.* **1992**, *72*, 3072.
 [33] N. Y. Garces, L. Wang, N. C. Giles, L. E. Halliburton, G. Cantwell, D. B. Eason, *J. Appl. Phys.* **2003**, *94*, 519.
 [34] Q. Mi, Y. Ping, Y. Li, B. Cao, B. S. Brunschwig, P. G. Khalifah, G. A. Galli, H. B. Gray, N. S. Lewis, *J. Am. Chem. Soc.* **2012**, *134*, 18318.

- [35] N. Ouldhamadouche, A. Achour, R. Lucio-Porto, M. Islam, S. Solaymani, A. Arman, A. Ahmadpourian, H. Achour, L. Le Brizoual, M. A. Djouadi, T. Brousse, *J. Mater. Sci. Technol.* **2018**, *34*, 976.
- [36] J.-C. Liu, J.-P. Chen, D.-Y. Li, *Acta Phys. Sin.* **1983**, *32*, 1053.
- [37] S. N. F. M. Nasir, H. Ullah, M. Ebadi, A. A. Tahir, J. S. Sagu, M. A. Mat Teridi, *J. Phys. Chem. C* **2017**, *121*, 6218.
- [38] P. F. Newhouse, D. Guevarra, M. Umehara, D. A. Boyd, L. Zhou, J. K. Cooper, J. A. Haber, J. M. Gregoire, *Chem. Commun.* **2019**, *55*, 489.
- [39] Q. Yan, J. Yu, S. K. Suram, L. Zhou, A. Shinde, P. F. Newhouse, W. Chen, G. Li, K. A. Persson, J. M. Gregoire, J. B. Neaton *Proc. Natl. Acad. Sci.* **2017**, *114*, 3040.
- [40] F. F. Abdi, N. Firet, *ChemCatChem* **2012**, *5*, 490.
- [41] F. F. Abdi, R. van de Krol, *J. Phys. Chem. C* **2012**, *116*, 9398.
- [42] Y. Q. Liang, T. Tsubota, L. P. A. Mooij, R. van de Krol, *J. Phys. Chem. C* **2011**, *115*, 17594.
- [43] J. F. Ziegler, M. D. Ziegler, J. P. Biersack, *Nucl. Instrum. Methods Phys. Res. Sect. B* **2010**, *268*, 1818.
- [44] G. Buxbaum, G. Pfaff, *Industrial Inorganic Pigments*, Wiley, Weinheim, Germany **2008**.
- [45] A. Ghosh, N. Kumari, A. Bhattacharjee, *Pramana* **2015**, *84*, 621.
- [46] G. Kresse, J. Hafner, *Phys. Rev. B* **1994**, *49*, 14251.
- [47] G. Kresse, J. Furthmüller, *Comput. Mater. Sci.* **1996**, *6*, 15.
- [48] J. P. Perdew, K. Burke, M. Ernzerhof, *Phys. Rev. Lett.* **1996**, *77*, 3865.
- [49] P. E. Blöchl, *Phys. Rev. B* **1994**, *50*, 17953.
- [50] H. J. Monkhorst, J. D. Pack, *Phys. Rev. B* **1976**, *13*, 5188.
- [51] B. Delley, *J. Chem. Phys.* **2000**, *113*, 7756.
- [52] B. Delley, *J. Chem. Phys.* **1990**, *92*, 508.
- [53] J.-W. Jang, D. Friedrich, S. Müller, M. Lamers, H. Hempel, S. Lardhi, Z. Cao, M. Harb, L. Cavallo, R. Heller, R. Eichberger, R. van de Krol, F. F. Abdi, *Adv. Energy Mater.* **2017**, *7*, 1701536.
- [54] J. Heyd, G. E. Scuseria, M. Ernzerhof, *J. Chem. Phys.* **2003**, *118*, 8207.
- [55] J. Heyd, G. E. Scuseria, M. Ernzerhof, *J. Chem. Phys.* **2006**, *124*, 219906.
- [56] J. Paier, M. Marsman, K. Hummer, G. Kresse, I. C. Gerber, J. G. Ángyán, *J. Chem. Phys.* **2006**, *124*, 154709.
- [57] S. Lardhi, D. Noureldine, M. Harb, A. Ziani, L. Cavallo, K. Takanabe, *J. Chem. Phys.* **2016**, *144*, 134702.
- [58] D. Noureldine, S. Lardhi, A. Ziani, M. Harb, L. Cavallo, K. Takanabe, *J. Mater. Chem. C* **2015**, *3*, 12032.
- [59] S. Lardhi, L. Cavallo, M. Harb, *J. Phys. Chem. C* **2018**, *122*, 18204.
- [60] M. Gajdoš, K. Hummer, G. Kresse, J. Furthmüller, F. Bechstedt, *Phys. Rev. B* **2006**, *73*, 45112.